



1 **Photochemical aging of aerosols contributes significantly to the**  
2 **production of atmospheric formic acid**

3 Yifan Jiang<sup>1</sup>, Men Xia<sup>2,3</sup>, Zhe Wang<sup>4</sup>, Penggang Zheng<sup>4</sup>, Yi Chen<sup>4</sup>, and Tao Wang<sup>1</sup>

4 <sup>1</sup>Department of Civil and Environmental Engineering, The Hong Kong Polytechnic University,  
5 Hong Kong SAR 999077, China

6 <sup>2</sup>Institute for Atmospheric and Earth System Research/Physics, Faculty of Science, University  
7 of Helsinki, Helsinki 00014, Finland

8 <sup>3</sup>Aerosol and Haze Laboratory, Advanced Innovation Center for Soft Matter Science and  
9 Engineering, Beijing University of Chemical Technology, 100029, Beijing, China

10 <sup>4</sup>Division of Environment and Sustainability, Hong Kong University of Science and  
11 Technology, Hong Kong SAR 999077, China

12 *Correspondence to:* Tao Wang (tao.wang@polyu.edu.hk)

13 **Abstract**

14 Formic acid (HCOOH) is one of the most abundant organic acids in the atmosphere and  
15 affects atmospheric acidity and aqueous chemistry. However, the formation mechanisms of  
16 HCOOH remain poorly understood, and current air-quality models largely underestimate  
17 observed atmospheric concentrations of HCOOH. In particular, HCOOH production from  
18 condensed-phase or heterogeneous reactions is not considered in current models. In a recent  
19 field study, we measured atmospheric HCOOH concentrations at a coastal site in South China.  
20 The average concentrations of HCOOH were  $191.1 \pm 167.2$  ppt in marine air masses and  $996.3$   
21  $\pm 432.9$  ppt in coastal air masses. A strong linear correlation between HCOOH concentrations  
22 and the surface area densities of submicron particulate matter was observed in coastal air  
23 masses. Post-campaign laboratory experiments confirmed that the photochemical aging of  
24 ambient aerosols promoted by heterogeneous reactions with ozone produced a high  
25 concentration of HCOOH at a rate of  $0.185$  ppb h<sup>-1</sup> under typical ambient conditions at noon  
26 time. HCOOH production was strongly affected by nitrate photolysis, as this efficiently  
27 produces OH radicals that oxidise organics to form HCOOH. We incorporated this particle-  
28 phase source into a photochemical model and found that it explained 81% of the peak  
29 concentration of ambient HCOOH and reproduced the diurnal variation in HCOOH  
30 concentrations. These findings demonstrate that the photochemical aging of aerosols is an  
31 important source of HCOOH that must be included in atmospheric chemistry-transport models.



## 32 1. Introduction

33 Organic acids are ubiquitous in the troposphere and constitute a significant fraction of the  
34 total organics in both the gas and particle phases (Chebbi & Carlier, 1996). They also  
35 participate in the aqueous-phase chemistry of clouds, contribute to secondary organic aerosol  
36 (SOA) formation through reactions within the condensed phase (Carlton et al., 2007; Ervens et  
37 al., 2004; Lim et al., 2010), and are proposed to enhance the formation of new particles in the  
38 atmosphere (Zhang et al., 2004). Formic acid (HCOOH) is among the most abundant organic  
39 acids in the atmosphere (Khare et al., 1999) and accounts for over 60% of the free acidity in  
40 precipitation in remote areas and more than 30% of that in polluted areas (Andreae et al., 1988;  
41 Keene et al., 1983; Keene & Galloway, 1988; Khare et al., 1999; Stavrakou et al., 2012). This  
42 contribution is increasingly important due to the decline in the concentrations of anthropogenic  
43 nitrogen oxides (NO<sub>x</sub>) and sulfur dioxide. HCOOH serves as a significant sink of in-cloud  
44 hydroxyl radicals ( $\cdot\text{OH}$ ) and stabilised Criegee intermediates (SCIs) (Jacob, 1986), and thus  
45 influences aqueous-phase chemistry by affecting pH-dependent reaction rates, oxidant  
46 concentrations, and solubilities (Vet et al., 2014). HCOOH also plays a role in the formation of  
47 cloud condensation nuclei (Yu, 2000), due to its comparatively higher hygroscopicity at low  
48 critical supersaturations when incorporated into aerosols (Novakov & Penner, 1993). This, in  
49 turn, affects total indirect radiative forcing. Additionally, HCOOH may be involved in halogen  
50 chemistry through its heterogeneous reaction with solid sodium chloride in sea-salt aerosols  
51 (Xia et al., 2018).

52 Considering the abovementioned roles of HCOOH in atmospheric chemistry, it is essential  
53 to understand its sources and sinks. However, the budget of HCOOH is currently poorly  
54 quantified, with state-of-the-art chemistry-transport models significantly underestimating  
55 field-observed concentrations of HCOOH (Baboukas et al., 2000; Bannan et al., 2017;  
56 Chaliyakunnel et al., 2016; Le Breton et al., 2012; Millet et al., 2015; Yuan et al., 2015).  
57 HCOOH is primarily removed from the atmosphere through wet and dry deposition, with a  
58 minor sink of being photo-oxidation by  $\cdot\text{OH}$  (Atkinson et al., 2006). The main sources of  
59 HCOOH include direct emissions from terrestrial vegetation (Andreae et al., 1988), biomass  
60 and biofuel burning (Akagi et al., 2011; Goode et al., 2000; Yokelson et al., 2009), fossil-fuel  
61 combustion (Kawamura et al., 2000; Zervas et al., 2001b, 2001a) and soil emissions (Sanhueza  
62 & Andreae, 1991). Moreover, secondary formation from the oxidation of volatile organic  
63 compounds (VOCs) is considered the major source of HCOOH at the global scale (Paulot et  
64 al., 2011). Despite the inclusion in models of various gas-phase mechanisms of HCOOH  
65 formation, such as ozonolysis of terminal alkenes (Neeb et al., 1997), alkyne oxidation (Bohn  
66 et al., 1996), OH-initiated isoprene oxidation (Paulot et al., 2009), monoterpene oxidation  
67 (Larsen et al., 2001), keto-enol tautomerisation (Andrews et al., 2012; Shaw et al., 2018)  
68 and  $\cdot\text{OH}$  oxidation of methylendioxy radicals (CH<sub>3</sub>O<sub>2</sub> $\cdot$ ) (Bossolasco et al., 2014), HCOOH



69 concentrations remain significantly underestimated (Millet et al., 2015; Yuan et al., 2015),  
70 indicating that a substantial missing source of HCOOH remains unidentified.

71 Current models do not consider HCOOH production from heterogeneous or condensed-  
72 phase reactions, but these could be an important source of HCOOH. Aqueous reactions of  
73 formaldehyde (HCHO) (Chameides & Davis, 1983; Jacob, 1986), glyoxal (Carlton et al., 2007),  
74 and other species with  $\cdot\text{OH}$  (aq) can produce HCOOH, particularly in moderately acidic  
75 environments (Jacob, 1986). A multiphase cloud-processing pathway involving methanediol  
76 oxidation was proposed that reconciles model predictions with measured concentrations of  
77 HCOOH (Franco et al., 2021). Moreover, Gao et al. (2022) recently proposed a new  
78 bidirectional deposition-emission process, whereby HCOOH deposits rapidly in night-time  
79 dew and is re-emitted from the dew as it evaporates on the following day. They found that this  
80 process explained most of the concentrations of HCOOH that they observed. Laboratory  
81 chamber studies have demonstrated that the photochemical aging of organic aerosols can also  
82 produce HCOOH (Henry & Donahue, 2012; Malecha & Nizkorodov, 2016; Mang et al., 2008;  
83 Pan et al., 2009; Walser et al., 2007; Zhang et al., 2021), but the importance of this process as  
84 a source of atmospheric HCOOH has not been quantified, and this source is not considered in  
85 current models.

86 The photochemical aging of aerosols occurs through the reactive uptake of oxidants onto  
87 particle surfaces, altering their chemical compositions and physical properties (George et al.,  
88 2015). In the condensed organic phase, this aging process can produce volatile compounds,  
89 such as HCOOH, through the photodegradation of SOA (Henry & Donahue, 2012; Malecha &  
90 Nizkorodov, 2016). Furthermore, the photolysis of particulate nitrate ( $\text{NO}_3^-$ ) produces oxidants  
91 such as  $\cdot\text{OH}$ , nitrogen dioxide ( $\text{NO}_2$ ), and nitrite ions/nitrous acid (HONO), which efficiently  
92 oxidise glyoxal to HCOOH (Zhang et al., 2021). Paulot et al. (2011) observed a marked positive  
93 correlation between HCOOH concentrations and submicron organic aerosol masses in three  
94 coastal, urban, and polar regions, and suggested that aerosol aging produces HCOOH. However,  
95 another field and model study estimated that this aging process makes only a minor (<5%)  
96 contribution to concentrations of HCOOH, although large uncertainties in the result were noted  
97 (Yuan et al., 2015). Overall, the aforementioned results show that there is a need for the  
98 determination of improved constraints on HCOOH production from the photochemical aging  
99 of aerosols, as this will enable assessment of the significance of this process as a source of  
100 HCOOH in comparison with other sources.

101 In this study, we measured HCOOH concentrations at near-ground level at a coastal site in  
102 Hong Kong, China, for 2 months during autumn 2021. We examined the characteristics of  
103 HCOOH concentrations and their correlation with related species' concentrations or other  
104 parameters. We showed that the use of current gas-phase mechanisms in a photochemical box  
105 model underpredicted the observed concentrations of HCOOH at our site. We then conducted  
106 a chamber study to measure the rate of HCOOH production during the aging of ambient



107 aerosols and extrapolated the results to the real atmosphere. We incorporated this HCOOH-  
108 formation mechanism into a model using a parameterisation involving fine particulate matter  
109 concentration, surface area density, light intensity, and ozone (O<sub>3</sub>) concentration, and then  
110 performed simulations to evaluate the contribution made by the photochemical aging of  
111 aerosols to HCOOH production. Furthermore, we showed that NO<sub>3</sub><sup>-</sup> photolysis acted as a  
112 crucial source of ·OH during the aging process. Our results enhance the understanding of  
113 HCOOH sources and model simulations of ambient HCOOH concentrations.

## 114 2. Methods

### 115 2.1. Field observations

116 Ambient measurements of the atmospheric concentrations of HCOOH and related  
117 species/parameters were conducted from 13 August to 31 October 2021 at the Hong Kong  
118 Environmental Protection Department's Cape D'Aguilar Super Site (CDSS; 22.21°N,  
119 114.25°E), which is situated a few hundred meters away from the nearest coastline of the South  
120 China Sea (Fig. S1). During the study period, this coastal site was initially predominantly  
121 influenced by marine air masses and subsequently by coastal air masses. The site was also  
122 affected by biogenic emissions (from deciduous and evergreen trees) and ship emissions (from  
123 ships in nearby waters). There were no other significant anthropogenic sources nearby.

124 The species quantified were HCOOH, HONO, trace gases (nitric oxide, NO<sub>2</sub>, carbon  
125 monoxide (CO), sulfur dioxide (SO<sub>2</sub>), and O<sub>3</sub>), volatile organic compounds (VOCs),  
126 oxygenated VOCs, aerosol mass concentrations (1-µm particulate matter (PM<sub>1</sub>), PM<sub>2.5</sub>, and  
127 PM<sub>10</sub> concentrations), aerosol size distributions, aerosol ionic compositions, NO<sub>2</sub> photolysis  
128 frequency (jNO<sub>2</sub>), and meteorological parameters (temperature (T), relative humidity (RH),  
129 wind direction, and wind speed). A detailed description of the measurement of HCOOH  
130 concentration is provided below, and information on other measurements is summarised in  
131 Table S1.

132 The concentration of HCOOH was measured at 172.91 atomic mass unit (amu) using an  
133 iodide-adduct time-of-flight chemical ionisation mass spectrometer (I<sup>-</sup>-ToF-CIMS, Aerodyne  
134 Research), as we used in our previous study at the same site (M. Xia et al., 2022). A  
135 comprehensive description of the use of the I<sup>-</sup>-ToF-CIMS can be found in previous studies  
136 (Aljawhary et al., 2013; Lee et al., 2014). Briefly, humidified iodomethane-containing N<sub>2</sub> air  
137 was passed through an inline ioniser (containing polonium-210) to generate iodide ions (I<sup>-</sup>) and  
138 iodide–water ions, which served as the reagent ions, and the HCOOH produced was detected  
139 as IHCOOH<sup>-</sup>. The background concentration of HCOOH was determined every 2 days by  
140 injecting zero air and was found to be 60.9 ppt. HCOOH calibration was performed three times  
141 on-site and once in the laboratory immediately following the field campaign using diluted gas  
142 standards generated by a permeation tube (KIN-TEK) with a permeation rate of 90.87 ng min<sup>-1</sup>



143 <sup>1</sup>. HCOOH sensitivity varies with RH as water competes with HCOOH for I<sup>-</sup> (Lee et al., 2014).  
144 Thus, the HCOOH sensitivity was measured at various RHs, as shown in Fig. S2. The  
145 sensitivity remained stable at a given RH, with a variation of less than 5% throughout the  
146 campaign.

147 The ToF-CIMS was housed in an air-conditioned shelter at an indoor air T maintained at  
148 25–28 °C. The shelter was located approximately 15 m away from the CDSS station. The  
149 sampling tube was a 0.5-m long perfluoroalkoxy-Teflon tube (1/2 in. outer diameter), the inlet  
150 of which was situated on the sidewall of the shelter, 1.5 m above the ground. To achieve laminar  
151 flow in the sampling tube, a flow rate of 25 Lpm was adopted, with a residence time of 0.1 s.  
152 The ToF-CIMS drew ~2 Lpm sample air, and the remaining airflow was discarded. The  
153 sampling tube was replaced with a new tube every 2 days to reduce inlet artifacts. We  
154 investigated possible inlet artifacts by injecting known concentrations of HCOOH into a used  
155 sampling inlet and found that the artifacts had a negligible effect on the measured HCOOH  
156 concentration (difference < 3%). The remaining instruments were housed in the CDSS station,  
157 with their sampling inlets located ~1.5 m above the roof.

158 2.2. Hybrid Single-Particle Lagrangian Integrated Trajectory (HYSPLIT) and Extended  
159 Aerosol Inorganic Model IV (E-AIM IV) models

160 Hourly 24-h backward trajectories were obtained using the HYSPLIT model  
161 (<https://www.ready.noaa.gov/hypub-bin/trajsrc.pl>). The input parameters were Global Data  
162 Assimilation System 1° for the meteorology data; 22.21°N and 114.25°E for the location; and  
163 100 m for the endpoint height, which is slightly higher than the site's altitude. Air masses were  
164 classified as marine or coastal, based on their source regions. A unique period was identified  
165 as a haze period, during which there was a transition from marine air masses to coastal air  
166 masses under stagnant conditions (wind speed < 3 m s<sup>-1</sup>). A detailed classification can be found  
167 in Fig. S3.

168 The aerosol water content (AWC) and pH were predicted by the E-AIM IV online in batch  
169 mode (<http://www.aim.env.uea.ac.uk/aim/model4/model4d.php>). The thermodynamic model  
170 was constrained by hourly field-measured molar concentrations of NH<sub>4</sub><sup>+</sup>, sodium ions (Na<sup>+</sup>),  
171 sulfate ions (SO<sub>4</sub><sup>2-</sup>), NO<sub>3</sub><sup>-</sup>, and chloride ions (Cl<sup>-</sup>) in PM<sub>2.5</sub>; gas-phase ammonia concentrations;  
172 ambient T; and RH. Initial concentrations of protons (H<sup>+</sup>) and hydroxide ions were estimated  
173 based on the ion balance of the major water-soluble ions. The input of Na<sup>+</sup> into the model  
174 (Na<sup>+(eq)</sup>) was calculated as a sum of the equivalent concentrations of Na<sup>+</sup>, potassium ions,  
175 magnesium ions, and calcium ions (Eq. (1)). The model also considered water dissociation and  
176 allowed all possible solids to form in the system. Parameters p, q, r, and s (options in batch  
177 mode) were set to 3, meaning that the input portions of ammonium (NH<sub>4</sub><sup>+</sup>), NO<sub>3</sub><sup>-</sup>, SO<sub>4</sub><sup>2-</sup>, and  
178 Cl<sup>-</sup> always remained in the condensed phase and did not produce corresponding gas-phase  
179 species, such as nitric acid (HNO<sub>3</sub>) and hydrochloric acid. The aqueous-phase NO<sub>3</sub><sup>-</sup>  
180 concentration was calculated by dividing the AWC by the moles of aqueous NO<sub>3</sub><sup>-</sup>. Aerosol pH



181 was calculated as the negative logarithm of the concentration of H<sup>+</sup>.

$$182 \quad [Na^+]_{eq} = [Na^+] + [K^+] + 2[Mg^{2+}] + 2[Ca^{2+}] \quad (1)$$

### 183 2.3. Chemical box model

184 The Framework for 0-D Atmospheric Modeling (F0AM version 4.2.1) (Wolfe et al., 2016)  
185 coupled with Master Chemical Mechanism (MCM v3.3.1, <http://mcm.york.ac.uk>) (Jenkin et  
186 al., 2015) was employed to investigate the formation of HCOOH at the field site. We followed  
187 Yuan et al. (2015) by enhancing the simulation of the secondary formation of HCOOH by  
188 modifying the HCOOH yields obtained by the ozonolysis of alkenes and other unsaturated  
189 species, and by adding chemical processes (vinyl alcohol oxidation; photo-tautomerisation of  
190 vinyl alcohol; and the reactions of HCHO + HO<sub>2</sub> and CH<sub>3</sub>O<sub>2</sub>· + ·OH) to the MCM. A single  
191 typical episode day, 28 September 2021, was selected as an example to run the model, as the  
192 critical model-input data were available on this day. The measured concentrations of O<sub>3</sub>, NO<sub>x</sub>,  
193 CO, SO<sub>2</sub>, HONO, VOCs, and OVOCs were averaged or interpolated to 5-min resolution and  
194 constrained in the model. We also run the model using hourly averaged data of another typical  
195 day in coastal air masses, 28 October 2021, and diurnal variations during the whole campaign.  
196 The methane concentration was assumed to remain constant (2000 ppb; Peng et al., 2022), due  
197 to a lack of measurement data. The dilution process was treated as a first-order loss with a  
198 dilution loss rate coefficient of 1/86,400 s<sup>-1</sup>, consistent with previous studies (Li et al., 2014;  
199 Yuan et al., 2015). The dry deposition rate was determined based on the deposition velocity  
200 and the boundary layer height (BLH). For HCOOH, a deposition velocity of 1 cm s<sup>-1</sup> was  
201 employed (Müller et al., 2018). A sensitivity analysis of the deposition velocity was also  
202 conducted. The diurnal profile of BLH was acquired from a previous study at another coastal  
203 site in Hong Kong (Su et al., 2017). Wet deposition was not considered as there was no rainfall  
204 on 28 September 2021. The model was executed for three replicates to stabilise the intermediate  
205 species it generated, and the results from the final run were used for further analysis. Primary  
206 emissions and transportation from other regions were not considered in the box model; thus,  
207 the production rate of HCOOH was utilised to evaluate the significance of various chemical  
208 pathways.

### 209 2.4. Laboratory experiments

210 We illuminated ambient aerosols collected on filters or aqueous solutions in a dynamic  
211 chamber to mimic HCOOH formation in the atmosphere. The overall experimental setup is  
212 illustrated in Fig. S4. The dynamic chamber has a dimension of 25-cm length × 15-cm width ×  
213 4-cm height with the top side sealed by a transparent Teflon film. Each aerosol filter or solution  
214 sample was placed in a quartz Petri dish (inner diameter: 35 mm, inner height: 7 mm) at the  
215 chamber's centre. Aerosol filter sampling details can be found in Text S1. A high-pressure  
216 xenon (Xe) lamp was used to simulate sunlight and its spectral irradiance is displayed in Fig.  
217 6d. Compared with standard air mass 1.5 solar irradiation (AM 1.5) corresponding to a solar  
218 zenith angle of 48.2°, the Xe lamp exhibited a smaller flux at 300–326 nm but a larger flux at



219 326–420 nm. An air stream from a zero-air generator (EnviroNics, model 7000) served as the  
220 carrier gas that delivered reaction products to the chamber’s outflow. The weather conditions  
221 that prevailed during the field campaign were mimicked by maintaining the reactor’s T at  
222 approximately 28 °C and adjusting the RH in the chamber to 70% by passing the carrier gas  
223 through a water bubbler. Prior to the introduction of a sample into the chamber, the background  
224 HCOOH concentration was monitored for 10 min with the light on and zero air added. After 1  
225 h of irradiation, 100 ppb of O<sub>3</sub> was introduced via a dynamic calibrator (EnviroNics® Series  
226 6100) and monitored using an O<sub>3</sub> analyser (Thermo Scientific Model 49i). An AM 1.5 filter  
227 (which removes light below 360 nm) and a 300–800 nm filter (which allows the passage of  
228 300–800 nm light) were applied to the Xe lamp to investigate the effect of the irradiation  
229 wavelength on the formation of HCOOH.

230 A sample solution was prepared by mixing formaldehyde (HCHO, Sigma-Aldrich, 37 wt%  
231 in water) and sodium nitrate (NaNO<sub>3</sub>, Honeywell, 99.5% purity). The resulting solution  
232 contained 0.15 wt% HCHO and 0.2 M NaNO<sub>3</sub>, and was adjusted to pH 2.7 by the addition of  
233 sulfuric acid (H<sub>2</sub>SO<sub>4</sub>, Sigma-Aldrich, 98% purity), as this was the E-AIM model’s prediction  
234 of the average aerosol acidity during the entire campaign. We assumed that ·OH produced by  
235 NO<sub>3</sub><sup>-</sup> photolysis was the rate-limiting species and HCHO was taken as an example of one of  
236 the possible precursors of HCOOH.

237 The average rate of production (ppb·s<sup>-1</sup>) of HCOOH (P<sub>HCOOH</sub>) during the 1-h irradiation  
238 was calculated by the following equation (Eq. (2)), derived from (Peng et al., 2022):

$$239 \quad P_{\text{HCOOH}} = \int_0^{60} (C_{\text{HCOOH}} - C_{\text{HCOOH-bkg}}) dt \times \frac{Q}{V} / 60 \quad (2)$$

240 where Q is the carrier gas flow rate (4 L min<sup>-1</sup>); V is the reactor chamber volume (1.875 L);  
241 and C<sub>HCOOH</sub> and C<sub>HCOOH-bkg</sub> (ppb) are the concentrations of HCOOH in the chamber after and  
242 before adding the sample, respectively. The photolytic loss of HCOOH was ignored, as the  
243 cross-section of HCOOH was beyond the spectral range of the Xe lamp (Burkholder et al.,  
244 2020).

245 We attempted to extrapolate the laboratory results to account for the field-observed  
246 concentrations of HCOOH. As photochemical aging occurs on aerosol surfaces and a strong  
247 correlation between the surface area (Sa) and the concentration of HCOOH observed in the  
248 field, the extrapolation was conducted based on Sa. The Sa in the chamber was calculated as  
249 the Sa of the filter divided by the chamber’s volume, assuming that only the first layer of the  
250 aerosols was illuminated. Although this might have resulted in an underestimation of the Sa  
251 density in the chamber, this assumption was reasonable, because particles in the lower layers  
252 would receive less light than those in the uppermost layer due to the light-screening effect of  
253 the first layer (Ye et al., 2017). The aging process was also influenced by light intensity, and as  
254 we discovered that the major oxidant was generated by the photolysis of particulate NO<sub>3</sub><sup>-</sup> (See  
255 **Results**, section 3), the light intensity was normalised based on the photolytic frequency of



256 aqueous  $\text{NO}_3^-$  ( $J_{\text{NO}_3^-(\text{aq})}$ ) due to the absence of an absorption coefficient for particulate  $\text{NO}_3^-$ .  
257 Although there is a redshift of the particulate  $\text{NO}_3^-$  absorption wavelength compared with the  
258 aqueous-phase  $\text{NO}_3^-$  absorption wavelength, our results should be reliable because we used  
259  $J_{\text{NO}_3^-(\text{aq})}$  as a reference for normalisation rather than for calculating an accurate  $J_{\text{NO}_3^-(\text{aq})}$  (Du  
260 & Zhu, 2011; Zhu et al., 2008). The  $J_{\text{NO}_3^-(\text{aq})}$  under the Xe lamp was  $8.85 \times 10^{-6} \text{ s}^{-1}$  and the  
261 daytime average  $J_{\text{NO}_3^-(\text{aq})}$  in the ambient air at our site was  $1.12 \times 10^{-5} \text{ s}^{-1}$  (Text S3). Both  
262  $J_{\text{NO}_3^-(\text{aq})}$  values were calculated assuming a quantum yield equal to 1. The normalised HCOOH  
263 production rate in the ambient air ( $P_{\text{HCOOH-nml}}$ ) was calculated using the following equation (Eq  
264 (3)):

$$265 \quad P_{\text{HCOOH-nml}} = P_{\text{HCOOH}} \times \frac{S_{\text{aamb}}}{S_{\text{acha}}} \times 1.266 \quad (3)$$

266 where  $S_{\text{aamb}}$  represents the field-measured Sa density;  $S_{\text{acha}}$  denotes the Sa density calculated  
267 for the chamber; and 1.266 is the ratio of the ambient  $J_{\text{NO}_3^-(\text{aq})}$  to the chamber  $J_{\text{NO}_3^-(\text{aq})}$ . For the  
268 aging process involving  $\text{O}_3$ , the photolytic rate constant of  $\text{O}_3$  generating  $\text{O}^1\text{D}$  ( $J_{\text{O}_3 \rightarrow \text{O}^1\text{D}}$ ) in the  
269 chamber ( $1.31 \times 10^{-5} \text{ s}^{-1}$ ) was also normalised to the average daytime  $J_{\text{O}_3 \rightarrow \text{O}^1\text{D}}$  ( $1.84 \times 10^{-5} \text{ s}^{-1}$ )  
270 under ambient conditions (Text S3). For the results of the aqueous solution, the  
271 concentrations of HCHO and  $\text{NO}_3^-$  were also normalised.

## 272 3. Results and Discussion

### 273 3.1. Field measurements of HCOOH concentrations

274 The field site was exposed to two distinct types of air masses; initially, it was largely  
275 exposed to marine air masses, and later to coastal air masses. Marine air masses ( $T = 29.4 \pm$   
276  $2.0 \text{ }^\circ\text{C}$ ,  $\text{RH} = 85.8 \pm 7.0 \%$ ) were warmer and more humid than coastal air masses ( $T = 25.7 \pm$   
277  $2.3 \text{ }^\circ\text{C}$ ,  $\text{RH} = 77.0 \pm 6.0 \%$ ), and exhibited low concentrations of  $\text{O}_3$  ( $15.0 \pm 8.9 \text{ ppb}$ ) and high  
278 concentrations of  $\text{NO}_x$  ( $6.2 \pm 4.5 \text{ ppb}$ ). Conversely, coastal air masses were characterised by  
279 high concentrations of  $\text{O}_3$  ( $53.6 \pm 14.2 \text{ ppb}$ ) and low concentrations of  $\text{NO}_x$  ( $1.9 \pm 1.6 \text{ ppb}$ ).  
280 The high concentrations of  $\text{NO}_x$  in the marine air masses are attributable to the emissions from  
281 ocean-going container ships that passed the site approximately 8 km to the south. A haze event  
282 occurred from 24 September to 2 October, due to a transition from marine to coastal air masses  
283 under stagnant conditions.  $\text{O}_3$  concentrations steadily increased during the first 5 days, peaked  
284 on 29 September, and remained high until the end of the haze period (Fig. 1). Therefore, the  
285 potential HCOOH formation mechanism was analysed separately for these three distinct  
286 periods.

287 Ambient HCOOH concentrations significantly varied during the three periods. The average  
288 HCOOH concentration in marine air masses was  $191.1 \pm 167.2 \text{ ppt}$ ; this was higher than those  
289 over the remote ocean, due to local emission sources, but significantly lower than those in  
290 urban environments (Table 1). In contrast, the ambient HCOOH concentrations in coastal air





291 masses were substantially higher, averaging  $996.3 \pm 432.9$  ppt, comparable with other  
292 measurements at rural or urban background sites. During the haze period, the concentrations  
293 of HCOOH displayed a pattern similar to the concentrations of  $O_3$ , with the daytime peak  
294 concentration increasing from 673.5 to 2789.9 ppt. A pronounced diurnal variation in the  
295 concentration of HCOOH was observed throughout the entire campaign, as illustrated in Fig.  
296 2, consistent with other studies (Millet et al., 2015; Yuan et al., 2015). HCOOH concentrations  
297 rapidly increased after sunrise, peaking at approximately 1 pm (local time), and then quickly  
298 decreasing in the late afternoon, due to the weaker sunlight and lower BLH than earlier in the  
299 day.

300 HCOOH is widely recognised as a secondary photochemical product. Table 2 presents the  
301 Pearson correlation coefficients  $R$  between the concentration of HCOOH and those of other air  
302 pollutants or other meteorological parameters during the three distinct periods. The  
303 concentration of  $HNO_3$  was strongly correlated with the concentration of HCOOH throughout  
304 the entire field campaign, consistent with other studies (Bannan et al., 2017; Millet et al., 2015).  
305 This finding suggests that HCOOH is predominantly generated through secondary  
306 photochemical mechanisms at this site, as  $HNO_3$  is a secondary photochemical product  
307 resulting from the reaction between  $\cdot OH$  and  $NO_2$ . The positive linear relationship between the  
308 concentrations of  $O_3$  and HCOOH also implies the secondary source of HCOOH.

309 A previous laboratory study revealed that HCOOH can be produced by the photochemical  
310 aging of aerosols (Malecha & Nizkorodov, 2016), which may be an important process in  
311 ambient air. In the coastal air masses and haze period, there was a strong correlation between  
312 the concentrations of HCOOH and PM, particularly between the concentrations of HCOOH  
313 and  $PM_{10}$ . This was also observed by Paulot et al. (2011) and suggests that HCOOH may be  
314 produced from PM. The  $Sa$  of  $PM_{10}$  was also highly correlated with the concentration of  
315 HCOOH in both coastal air masses and haze periods, indicating that HCOOH is mainly  
316 produced from reactions on aerosol surfaces. However, in the marine air masses, the  
317 concentration of HCOOH was not related to aerosols due to the low particle concentrations in  
318 such masses. To further explore the potential role of aerosol aging in HCOOH production, we  
319 plotted the correlation of HCOOH concentrations with  $Sa \times O_3$ ,  $Sa \times NO_3^-$ , and  $Sa \times O_3 \times NO_3^-$   
320 for the coastal air masses (Fig. 3). We discovered that the correlation coefficient significantly  
321 increased when  $Sa$  was combined with the concentration of  $O_3$  or  $NO_3^-$  or with the  
322 concentrations of both species, compared with these three factors being considered separately.  
323 This finding suggests that the HCOOH observed in the coastal air masses was not  
324 predominantly derived from gas-phase  $O_3$  oxidation of VOCs; rather, it was derived from  
325 heterogeneous or condensed-phase reactions on aerosol surfaces. The results during the haze  
326 period were similar. Therefore, photochemical aerosol aging may play a key role in HCOOH  
327 production as the aging process involves the reactive uptake of oxidants onto particle surfaces.



### 328 3.2. Box model simulation

329 A box model was utilised to evaluate the formation mechanisms of HCOOH using the  
330 measurement data from a typical haze day (28 September 2021). The peak HCOOH  
331 concentration on that day was approximately 2 ppb, and occurred at approximately 3:30 pm.  
332 The base model, incorporating only the default mechanism of MCM v3.3.1, significantly  
333 underestimated the HCOOH concentration: the highest simulated concentration was 0.256 ppb,  
334 representing only 14.5% of the observed value. We made modifications to the formation  
335 mechanisms following Yuan et al. (2015) and these resulted in the simulated peak daytime  
336 concentration increasing to 0.363 ppb, accounting for 20.1% of the observed value (Fig. 4).  
337 Therefore, an additional HCOOH formation mechanism is required to account for the  
338 difference between the measured and simulated values.

339 A comprehensive analysis of HCOOH sources and sinks was conducted for both the base  
340 and modified cases (Fig. 5a & 5b). The reaction of CH<sub>2</sub>OO Criegee intermediate biradicals  
341 with H<sub>2</sub>O was identified as the major source of HCOOH, accounting for over 90% of the  
342 current known sources for both cases. CH<sub>2</sub>OO is formed from seven excited biradicals that  
343 originate from the O<sub>3</sub> oxidation of various alkenes and unsaturated compounds (Saunders et al.,  
344 2003). Among these, CH<sub>2</sub>OOE is the largest contributor to the production of CH<sub>2</sub>OO (Fig. S5)  
345 and is generated by the ozonolysis of isoprene. The primary loss of HCOOH is via deposition,  
346 owing to its high solubility in water. To account for uncertainty in the deposition velocity ( $V_d$ )  
347 of HCOOH, we conducted a sensitivity test of HCOOH production to various  $V_d$  values (Fig.  
348 5d). The results revealed that the simulated HCOOH concentration was insensitive to  $V_d$  when  
349 it was higher than 1.00 cm s<sup>-1</sup>. The daytime peak concentration increased by 60% when  $V_d$   
350 decreased from 1.00 to 0.50 cm s<sup>-1</sup>, but the model still largely underestimated the HCOOH  
351 concentration. The field-observed  $V_d$  of HCOOH ranges from 0.43 cm s<sup>-1</sup> to 1.10 cm s<sup>-1</sup> (Müller  
352 et al., 2018), and thus given the high humidity at the study site, the observed  $V_d$  of HCOOH of  
353 0.5 cm s<sup>-1</sup> should have been close to the lower limit. The simulated net HCOOH production  
354 (sources – sinks) became positive at approximately 9 am, while the ambient concentration of  
355 HCOOH started increasing at 6 am, which is aligned with sunrise (Fig. 2). These results  
356 indicate that there are pathways for the photochemical generation of HCOOH that are distinct  
357 from O<sub>3</sub> oxidation and these may include the photochemical aging of aerosols. We also  
358 executed the model on 28 October 2021, another day that was exposed to coastal air masses,  
359 and obtained similar outcomes (Fig. S6).

### 360 3.3. Laboratory experiments

361 Figure 6a presents the results of a typical aerosol-filter irradiation experiment. Upon turning  
362 on the light, HCOOH was instantaneously produced, indicating a rapid transfer from the  
363 condensed-phase to the gas phase through photochemical reactions. Within 3 minutes, the  
364 HCOOH concentration reached 11.1 ppb, but when the light was turned off, the HCOOH  
365 concentration quickly returned to nearly background concentrations. This suggests that



366 HCOOH was produced predominantly via photochemical reactions. The HCOOH  
367 concentration exhibited a logarithmic decay after its first peak concentration and this decay  
368 also occurred continued after its second peak concentration, which may be attributable to either  
369 the evaporative loss of HCOOH or the photochemical loss of oxidants (Ye et al., 2017). When  
370 the AM 1.5 filter was added, the HCOOH concentration decreased by approximately 48.1%  
371 within 5 min, and after the filter was removed, the HCOOH concentration returned to the  
372 logarithmic decay line. This suggests that there was only minor evaporation of HCOOH from  
373 the condensed-phase due to the increased temperature of aerosol surfaces under light irradiation.  
374 However, the addition of the 300–800 nm filter reduced the HCOOH concentration by only  
375 13.2%, indicating that the photochemical production of HCOOH primarily occurs at  
376 wavelengths lower than 360 nm. Given the agreement between the wavelength at which  $\text{NO}_3^-$   
377 absorbs light (290–350 nm) and the wavelength of HCOOH production (<360 nm), and the  
378 high correlation between the ambient HCOOH concentration and the product of Sa density and  
379  $\text{NO}_3^-$  concentration (as shown in Fig. 3), we infer that  $\cdot\text{OH}$  produced from  $\text{NO}_3^-$  photolysis  
380 were the major oxidants in the particle phase and thus drove HCOOH production. The  
381 production of HCOOH was also found to be dependent on  $\text{O}_3$ , as the concentration of HCOOH  
382 increased by 64.7% after the addition of 100 ppb of  $\text{O}_3$ .

383 We next extrapolated the production rate of HCOOH observed in the chamber to ambient  
384 conditions, using the method described in Section 2.4, to assess the role played by the  
385 photochemical aging of aerosols in HCOOH production. Table 3 summarises the HCOOH  
386 concentrations and production rates observed in the chamber experiments, and the normalised  
387 HCOOH production rates in ambient air under light and light +  $\text{O}_3$  conditions, respectively.  
388 The average  $P_{\text{HCOOH-nml}}$  without the addition of  $\text{O}_3$  was determined to be  $0.106 \text{ ppb h}^{-1}$ ,  
389 equivalent to 138.5% of the peak HCOOH production rate in the modified case. The addition  
390 of 100 ppb of  $\text{O}_3$  increased  $P_{\text{HCOOH-nml}}$  by  $0.079 \text{ ppb h}^{-1}$ , indicating that the heterogenous  
391 reaction between  $\text{O}_3$  and aerosols made a non-negligible contribution to HCOOH production.  
392 By comparing the net  $P_{\text{HCOOH-nml}}$  via the photochemical aging pathway with and without  $\text{O}_3$ , it  
393 was found that the incorporation of these two conditions into the model should improve the  
394 model results by factors of 2.89 and 1.51, respectively. These results highlight the importance  
395 of HCOOH production via the aging of aerosols, which we found generated more HCOOH  
396 than gas-phase reactions at our observation site.

397 We established a relationship between  $P_{\text{HCOOH-nml}}$  and three parameters:  $\text{PM}_{2.5}$   
398 concentration (cPM), which represents the reactant concentration; Sa, which represents the  
399 available reaction area; and  $j\text{NO}_2$ , which represents the light intensity. After multiplying these  
400 three factors, we discovered a strong linear correlation between  $P_{\text{HCOOH-nml}}$  and  $\text{cPM} \times \text{Sa} \times$   
401  $j\text{NO}_2$  (Fig. 6b). The intercept was set to zero, as there should be no HCOOH production when  
402  $\text{cPM} \times \text{Sa} \times j\text{NO}_2$  is zero. Based on the correlation, we derived an equation (Eq. (4)) for  
403 calculating  $P_{\text{HCOOH-nml}}$ . Additionally, we assumed that  $P_{\text{HCOOH-nml}(\text{O}_3)}$  increased linearly with  $\text{O}_3$



404 concentration. Incorporating this equation into the F0AM model by treating the photochemical  
405 production of HCOOH from particles as an emission resulted in significantly improved  
406 predictions: they explained 81% of the peak concentration, as illustrated by the black line in  
407 Figure 4. The production of HCOOH from particles was the largest source of HCOOH,  
408 accounting for 76% of the total production (Fig. 5c). Moreover, the model also reproduced a  
409 rapid increase in the concentration of HCOOH in the morning and a sharp decrease in the  
410 concentration of HCOOH in the late afternoon (Fig. 4). The different trend at midnight is  
411 attributable to the continuous deposition of HCOOH concomitant with no production in the  
412 model at that time. We also evaluated the model's performance in simulating HCOOH  
413 production for 28 October 2021. The particle-phase production narrowed the gap significantly  
414 and constituted over 70% of the total production (Fig. S6), which is consistent with the results  
415 for 28 September 2021.

416 In summary, the inclusion of HCOOH production from the photochemical aging of aerosols  
417 significantly improved the performance of the model. Although there may be limitations to the  
418 assumptions made in the parameterisation, particularly in environments containing with  
419 different chemical compositions of particles, this new parameterisation provides a general form  
420 constrained by four factors for calculating HCOOH production from the condensed phase.

$$421 \quad P_{\text{HCOOH-nml}} = 0.0091x + 0.010_3 \times 0.0064x, \quad x = \text{cPM} \times \text{Sa} \times j\text{NO}_2 \quad (4)$$

422 Photolysis of particulate  $\text{NO}_3^-$  is an important source of  $\cdot\text{OH}$  (Mack & Bolton, 1999;  
423 Zellner et al., 1990). To investigate the potential production of HCOOH from this source, an  
424 irradiation experiment was conducted on a solution (Fig. 6c). The concentration of HCOOH  
425 increased linearly with time and did not reach a stable state after 90 min of illumination. This  
426 differs from the aerosol experiments and might have been due to the continuous evaporation of  
427 water from the solution caused by the heating effect of the light source, which would have  
428 concentrated the solution. To determine the appropriate time to calculate  $P_{\text{HCOOH}}$ , we also  
429 plotted the time series of HONO concentrations. This showed that the HONO concentration  
430 stabilised after 1 h of irradiation, suggesting that  $\text{NO}_3^-$  photolysis also reached a steady state.  
431 As  $\cdot\text{OH}$  produced from  $\text{NO}_3^-$  photolysis were the only oxidants present in the system, the actual  
432 HCOOH production rate at the initial HCHO concentration should have followed the same  
433 trend as the HONO concentration. Therefore, we chose 1 h after turning on the light as the  
434 appropriate time to quantify  $P_{\text{HCOOH}}$ , and found that at this time,  $P_{\text{HCOOH}}$  in the chamber was  
435  $21.9 \text{ ppt s}^{-1}$ . We also attempted to extrapolate the results to ambient air, similar to the aerosol  
436 filter experiments. To do so, in addition to normalising Sa and light intensity, we needed to  
437 normalise the HCHO and  $\text{NO}_3^-$  concentrations. The average concentration of gas-phase HCHO  
438 ( $\text{HCHO}_{(g)}$ ) measured on 28 September was  $2.35 \mu\text{g cm}^{-3}$ . By using a ratio of 0.03 between the  
439 concentration of HCHO in the particle phase ( $\text{HCHO}_{(p)}$ ) and the concentration of HCHO in the  
440 gas phase (Toda et al., 2014), the concentration of  $\text{HCHO}_{(p)}$  was calculated to be  $0.07 \mu\text{g cm}^{-3}$ ,  
441 which is comparable to the concentrations that have been reported in previous studies (Klippel



442 & Warneck, 1980; Toda et al., 2014). Based on the aqueous volume of aerosol calculated by  
443 the E-AIM model ( $0.02 \mu\text{l m}^{-3}$ ), the HCHO mass concentration in the aqueous phase was found  
444 to be  $3.5 \text{ g L}^{-1}$ . The  $\text{NO}_3^-$  concentration on the aerosol surface was determined to be  $0.98 \text{ mol}$   
445  $\text{L}^{-1}$ . Therefore, the  $P_{\text{HCOOH}}$  in ambient air attributable to the aqueous oxidation of HCHO was  
446 estimated to be  $0.41 \text{ ppb h}^{-1}$ , which is 285% higher than the  $P_{\text{HCOOH}}$  attributable to the  
447 photochemical aging of ambient particles. This greater-than-100% contribution could be  
448 attributable to the simplicity of the solution system. In ambient air, other oxidisable species,  
449 such as halides (Peng et al., 2022; M. Xia et al., 2022) could also react with the  $\cdot\text{OH}$  produced  
450 from  $\text{NO}_3^-$  photolysis, which competes with HCHO. In summary,  $\text{NO}_3^-$  photolysis appears to  
451 be a critical source of oxidants during the photochemical aging process of aerosols.

#### 452 4. Conclusion and implications

453 This study provides the first estimate of high rates of HCOOH production from the  
454 photochemical aging of real ambient particles and demonstrates the potential importance of  
455 this pathway in the formation of HCOOH under ambient conditions at a coastal site in Hong  
456 Kong. Incorporating aerosol photochemical aging significantly improved the performance of a  
457 widely used chemical model, which underscores the significance of condensed-phase  
458 photochemistry and the necessity of incorporating its mechanisms into atmospheric models.  
459 The substantial production of HCOOH from condensed-phase photochemical reactions altered  
460 both the composition and the volatility of SOA. Moreover, other low-molecular-weight organic  
461 acids, such as acetic acid, may be produced via this mechanism, as observed in our irradiation  
462 experiments. Improving the constraints on this photochemical aging of aerosols will not only  
463 aid the understanding of the budget of these organic acids but also affect their SOA chemistry.

464 Our solution irradiation experiments demonstrated the importance of  $\text{NO}_3^-$  photolysis in  
465 HCOOH production via the production of  $\cdot\text{OH}$ . This suggests that  $\text{NO}_3^-$  photolysis not only  
466 influences the aerosol-based production of inorganic species (such as HONO (Ye et al., 2017)  
467 and halogens (Peng et al., 2022; M. Xia et al., 2022), but also the aerosol-based production of  
468 organics, particularly water-soluble organics. Thus, there is a need for future studies on the  
469 roles of  $\text{NO}_3^-$  photodissociation in aerosol aging processes, as such research would improve  
470 our understanding of the aging mechanisms of the condensed phase.

#### 471 Data availability

472 The data that support the findings of this study are openly available in Zenodo at  
473 <https://doi.org/10.5281/zenodo.8059231>. Other raw data are also available from the  
474 corresponding author, upon reasonable request.



## 475 Authors' contributions

476 T. W. arranged the field campaign and designed the laboratory irradiation experiment. Y. J. and  
477 M. X. conducted the field campaign and photochemical filter experiments. M. X. revised the  
478 model code. Y. J. conducted the photochemical solution experiments, analysed the data, ran the  
479 model, and wrote the draft manuscript. T. W. and M. X. revised the manuscript.

## 480 Competing interests

481 One author (Tao Wang) is a member of the editorial board of Atmospheric Chemistry and  
482 Physics. The authors have no other competing interests to declare.

## 483 Acknowledgements

484 We thank the Hong Kong Environmental Protection Department for allowing us to use the field  
485 study site and for providing data on VOCs, OVOCs, trace gases, PM mass concentrations, and  
486 ion compositions; the Hong Kong Observatory for providing the meteorological data; the Hong  
487 Kong Polytechnic University Research Facility in Chemical and Environmental Analysis for  
488 providing the ToF-CIMS; and Dr Zhao Jue for providing PM<sub>2.5</sub> filters, whose work is supported  
489 by projects (PolyU Project of Strategic Importance No. ZE2K and RGC-GRF No. 15203920).  
490 We are grateful to Steven Poon for his help with logistics.

## 491 Funding

492 This work was supported by the Research Grants Council of the Hong Kong (Project No.  
493 T24/504/17).

## 494 References

- 495 Akagi, S. K., Yokelson, R. J., Wiedinmyer, C., Alvarado, M. J., Reid, J. S., Karl, T., Crounse,  
496 J. D., & Wennberg, P. O. (2011). Atmospheric Chemistry and Physics Emission factors for open  
497 and domestic biomass burning for use in atmospheric models. *Atmos. Chem. Phys.*, 11, 4039–  
498 4072. <https://doi.org/10.5194/acp-11-4039-2011>
- 499 Aljawhary, D., Lee, A. K. Y., & Abbatt, J. P. D. (2013). High-resolution chemical ionization  
500 mass spectrometry (ToF-CIMS): Application to study SOA composition and processing.  
501 *Atmospheric Measurement Techniques*, 6(11), 3211–3224. <https://doi.org/10.5194/amt-6-3211-2013>
- 502  
503 Andreae, M. O., Talbot, R. W., Andreae, T. W., & Harriss, R. C. (1988). Formic and acetic acid  
504 over the central Amazon region, Brazil: 1. Dry season. *Journal of Geophysical Research:*  
505 *Atmospheres*, 93(D2), 1616–1624. <https://doi.org/10.1029/JD093ID02P01616>



- 506 Andrews, D. U., Heazlewood, B. R., Maccarone, A. T., Conroy, T., Payne, R. J., Jordan, M. J.  
507 T., & Kable, S. H. (2012). Photo-tautomerization of acetaldehyde to vinyl alcohol: A potential  
508 route to tropospheric acids. *Science*, 337(6099), 1203–1206.  
509 <https://doi.org/10.1126/SCIENCE.1220712>
- 510 Atkinson, R., Baulch, D. L., Cox, R. A., Crowley, J. N., Hampson, R. F., Hynes, R. G., Jenkin,  
511 M. E., Rossi, M. J., & Troe, J. (2006). Evaluated kinetic and photochemical data for  
512 atmospheric chemistry: Volume II - Gas phase reactions of organic species. *Atmospheric  
513 Chemistry and Physics*, 6(11), 3625–4055. <https://doi.org/10.5194/ACP-6-3625-2006>
- 514 Baboukas, E. D., Kanakidou, M., & Mihalopoulos, N. (2000). Carboxylic acids in gas and  
515 particulate phase above the Atlantic Ocean. *Journal of Geophysical Research: Atmospheres*,  
516 105(D11), 14459–14471. <https://doi.org/10.1029/1999JD900977>
- 517 Bannan, T. J., Murray Booth, A., le Breton, M., Bacak, A., Muller, J. B. A., Leather, K. E.,  
518 Khan, M. A. H., Lee, J. D., Dunmore, R. E., Hopkins, J. R., Fleming, Z. L., Sheps, L., Taatjes,  
519 C. A., Shallcross, D. E., & Percival, C. J. (2017). Seasonality of Formic Acid (HCOOH) in  
520 London during the ClearfLo Campaign. *Journal of Geophysical Research: Atmospheres*,  
521 122(22), 12,488–12,498. <https://doi.org/10.1002/2017JD027064>
- 522 Bohn, B., Siese, M., & Zetzsch, C. (1996). Kinetics of the OH + C<sub>2</sub>H<sub>2</sub> reaction in the presence  
523 of O<sub>2</sub>. *Journal of the Chemical Society, Faraday Transactions*, 92(9), 1459–1466.  
524 <https://doi.org/10.1039/FT9969201459>
- 525 Bossolasco, A., Faragó, E. P., Schoemaeker, C., & Fittschen, C. (2014). Rate constant of the  
526 reaction between CH<sub>3</sub>O<sub>2</sub> and OH radicals. *Chemical Physics Letters*, 593, 7–13.  
527 <https://doi.org/10.1016/J.CPLETT.2013.12.052>
- 528 Burkholder, J. B., Sander, S. P., Abbatt, J. P. D., Barker, J. R., Cappa, C., Crouse, J. D., Dibble,  
529 T. S., Huie, R. E., Kolb, C. E., Kurylo, M. J., Orkin, V. L., Percival, C. J., Wilmouth, D. M., &  
530 Wine, P. H. (2020). Chemical kinetics and photochemical data for use in atmospheric studies;  
531 evaluation number 19. <https://trs.jpl.nasa.gov/handle/2014/49199>
- 532 Carlton, A. G., Turpin, B. J., Altieri, K. E., Seitzinger, S., Reff, A., Lim, H. J., & Ervens, B.  
533 (2007a). Atmospheric oxalic acid and SOA production from glyoxal: Results of aqueous  
534 photooxidation experiments. *Atmospheric Environment*, 41(35), 7588–7602.  
535 <https://doi.org/10.1016/J.ATMOSENV.2007.05.035>
- 536 Chaliyakunnel, S., Millet, D. B., Wells, K. C., Cady-Pereira, K. E., & Shephard, M. W. (2016).  
537 A Large Underestimate of Formic Acid from Tropical Fires: Constraints from Space-Borne  
538 Measurements. *Environmental Science and Technology*, 50(11), 5631–5640.  
539 <https://doi.org/10.1021/acs.est.5b06385>
- 540 Chameides, W. L., & Davis, D. D. (1983). Aqueous-phase source of formic acid in clouds.  
541 *Nature* 1983 304:5925, 304(5925), 427–429. <https://doi.org/10.1038/304427a0>
- 542 Chebbi, A., & Carlier, P. (1996). Carboxylic acids in the troposphere, occurrence, sources, and  
543 sinks: A review. *Atmospheric Environment*, 30(24), 4233–4249. [15](https://doi.org/10.1016/1352-</a></p></div><div data-bbox=)



- 544 2310(96)00102-1
- 545 Chen, X., Millet, D. B., Neuman, J. A., Veres, P. R., Ray, E. A., Commane, R., Daube, B. C.,  
546 McKain, K., Schwarz, J. P., Katich, J. M., Froyd, K. D., Schill, G. P., Kim, M. J., Crouse, J.  
547 D., Allen, H. M., Apel, E. C., Hornbrook, R. S., Blake, D. R., Nault, B. A., ... Dibb, J. E. (2021).  
548 HCOOH in the Remote Atmosphere: Constraints from Atmospheric Tomography (ATom)  
549 Airborne Observations. *ACS Earth and Space Chemistry*, 5(6), 1436–1454.  
550 <https://doi.org/10.1021/acsearthspacechem.1c00049>
- 551 Du, J., & Zhu, L. (2011). Quantification of the absorption cross sections of surface-adsorbed  
552 nitric acid in the 335–365 nm region by Brewster angle cavity ring-down spectroscopy.  
553 *Chemical Physics Letters*, 511(4–6), 213–218. <https://doi.org/10.1016/j.cplett.2011.06.062>
- 554 Ervens, B., Feingold, G., Frost, G. J., & Kreidenweis, S. M. (2004). A modeling study of  
555 aqueous production of dicarboxylic acids: 1. Chemical pathways and speciated organic mass  
556 production. *Journal of Geophysical Research: Atmospheres*, 109(D15).  
557 <https://doi.org/10.1029/2003JD004387>
- 558 Fulgham, S. R., Brophy, P., Link, M., Ortega, J., Pollack, I., & Farmer, D. K. (2019). Seasonal  
559 Flux Measurements over a Colorado Pine Forest Demonstrate a Persistent Source of Organic  
560 Acids. *ACS Earth and Space Chemistry*, 3(9), 2017–2032.  
561 <https://doi.org/10.1021/acsearthspacechem.9b00182>
- 562 George, C., Ammann, M., D’Anna, B., Donaldson, D. J., & Nizkorodov, S. A. (2015).  
563 Heterogeneous Photochemistry in the Atmosphere. *Chemical Reviews*, 115(10), 4218–4258.  
564 <https://doi.org/10.1021/CR500648Z>
- 565 Goode, J. G., Yokelson, R. J., Ward, D. E., Susott, R. A., Babbitt, R. E., Davies, M. A., & Hao,  
566 W. M. (2000). Measurements of excess O<sub>3</sub>, CO<sub>2</sub>, CO, CH<sub>4</sub>, C<sub>2</sub>H<sub>4</sub>, C<sub>2</sub>H<sub>2</sub>, HCN, NO, NH<sub>3</sub>,  
567 HCOOH, CH<sub>3</sub>COOH, HCHO, and CH<sub>3</sub>OH in 1997 Alaskan biomass burning plumes by  
568 airborne Fourier transform infrared spectroscopy (AFTIR). *Journal of Geophysical Research:*  
569 *Atmospheres*, 105(D17), 22147–22166. <https://doi.org/10.1029/2000JD900287>
- 570 Henry, K. M., & Donahue, N. M. (2012). Photochemical aging of  $\alpha$ -pinene secondary organic  
571 aerosol: Effects of OH radical sources and photolysis. *Journal of Physical Chemistry A*,  
572 116(24), 5932–5940. <https://doi.org/10.1021/JP210288S>
- 573 Jacob, D. J. (1986). Chemistry of OH in remote clouds and its role in the production of formic  
574 acid and peroxymonosulfate. *Journal of Geophysical Research*, 91(D9), 9807.  
575 <https://doi.org/10.1029/JD091ID09P09807>
- 576 Jenkin, M. E., Young, J. C., & Rickard, A. R. (2015). The MCM v3.3.1 degradation scheme for  
577 isoprene. *Atmospheric Chemistry and Physics*, 15(20), 11433–11459.  
578 <https://doi.org/10.5194/ACP-15-11433-2015>
- 579 Kawamura, K., Steinberg, S., & Kaplan, I. R. (2000). Homologous series of C<sub>1</sub>–C<sub>10</sub>  
580 monocarboxylic acids and C<sub>1</sub>–C<sub>6</sub> carbonyls in Los Angeles air and motor vehicle exhausts.  
581 *Atmospheric Environment*, 34(24), 4175–4191. [16](https://doi.org/10.1016/S1352-</a></p></div><div data-bbox=)





- 582 2310(00)00212-0
- 583 Keene, W. C., & Galloway, J. N. (1988). The biogeochemical cycling of formic and acetic acids  
584 through the troposphere: an overview of current understanding. *Chemical and Physical*  
585 *Meteorology*, 40(5), 322–334. <https://doi.org/10.3402/tellusb.v40i5.15994>
- 586 Keene, W. C., Galloway, J. N., & Holden, J. D. (1983). Measurement of weak organic acidity  
587 in precipitation from remote areas of the world. *Journal of Geophysical Research*, 88(C9),  
588 5122–5130. <https://doi.org/10.1029/JC088IC09P05122>
- 589 Khare, P., Kumar, N., Kumari, K. M., & Srivastava, S. S. (1999). Atmospheric formic and  
590 acetic acids: An overview. *Reviews of Geophysics*, 37(2), 227–248.  
591 <https://doi.org/10.1029/1998RG900005>
- 592 Klippel, W., & Warneck, P. (1980). The formaldehyde content of the atmospheric aerosol.  
593 *Atmospheric Environment* (1967), 14(7), 809–818. [https://doi.org/10.1016/0004-](https://doi.org/10.1016/0004-6981(80)90137-7)  
594 [6981\(80\)90137-7](https://doi.org/10.1016/0004-6981(80)90137-7)
- 595 Larsen, B. R., di Bella, D., Glasius, M., Winterhalter, R., Jensen, N. R., & Hjorth, J. (2001).  
596 Gas-Phase OH Oxidation of Monoterpenes: Gaseous and Particulate Products. *Journal of*  
597 *Atmospheric Chemistry* 2001 38:3, 38(3), 231–276. <https://doi.org/10.1023/A:1006487530903>
- 598 le Breton, M., McGillen, M. R., Muller, J. B. A., Bacak, A., Shallcross, D. E., Xiao, P., Huey,  
599 L. G., Tanner, D., Coe, H., & Percival, C. J. (2012). Airborne observations of formic acid using  
600 a chemical ionization mass spectrometer. *Atmospheric Measurement Techniques*, 5(12), 3029–  
601 3039. <https://doi.org/10.5194/amt-5-3029-2012>
- 602 Lee, B. H., Lopez-Hilfiker, F. D., Mohr, C., Kurtén, T., Worsnop, D. R., & Thornton, J. A.  
603 (2014). An iodide-adduct high-resolution time-of-flight chemical-ionization mass spectrometer:  
604 Application to atmospheric inorganic and organic compounds. *Environmental Science and*  
605 *Technology*, 48(11), 6309–6317. <https://doi.org/10.1021/es500362a>
- 606 Li, X., Rohrer, F., Brauers, T., Hofzumahaus, A., Lu, K., Shao, M., Zhang, Y. H., & Wahner, A.  
607 (2014). Modeling of HCHO and CHOCHO at a semi-rural site in southern China during the  
608 PRIDE-PRD2006 campaign. *Atmospheric Chemistry and Physics*, 14(22), 12291–12305.  
609 <https://doi.org/10.5194/ACP-14-12291-2014>
- 610 Lim, Y. B., Tan, Y., Perri, M. J., Seitzinger, S. P., & Turpin, B. J. (2010). Aqueous chemistry  
611 and its role in secondary organic aerosol (SOA) formation. *Atmospheric Chemistry and Physics*,  
612 10(21), 10521–10539. <https://doi.org/10.5194/ACP-10-10521-2010>
- 613 Mack, J., & Bolton, J. R. (1999). Photochemistry of nitrite and nitrate in aqueous solution: a  
614 review. *Journal of Photochemistry and Photobiology A: Chemistry*, 128(1–3), 1–13.  
615 [https://doi.org/10.1016/S1010-6030\(99\)00155-0](https://doi.org/10.1016/S1010-6030(99)00155-0)
- 616 Malecha, K. T., & Nizkorodov, S. A. (2016). Photodegradation of Secondary Organic Aerosol  
617 Particles as a Source of Small, Oxygenated Volatile Organic Compounds.  
618 <https://doi.org/10.1021/acs.est.6b02313>
- 619 Mang, S. A., Henricksen, D. K., Bateman, A. E., Andersen, M. P. S., Blake, D. R., &



- 620 Nizkorodov, S. A. (2008). Contribution of carbonyl photochemistry to aging of atmospheric  
621 secondary organic aerosol. *Journal of Physical Chemistry A*, 112(36), 8337–8344.  
622 <https://doi.org/10.1021/JP804376C>
- 623 Millet, D. B., Baasandorj, M., Farmer, D. K., Thornton, J. A., Baumann, K., Brophy, P.,  
624 Chaliyakunnel, S., de Gouw, J. A., Graus, M., Hu, L., Koss, A., Lee, B. H., Lopez-Hilfiker, F.  
625 D., Neuman, J. A., Paulot, F., Peischl, J., Pollack, I. B., Ryerson, T. B., Warneke, C., ... Xu, J.  
626 (2015). A large and ubiquitous source of atmospheric formic acid. *Atmospheric Chemistry and*  
627 *Physics*, 15(11), 6283–6304. <https://doi.org/10.5194/acp-15-6283-2015>
- 628 Miyazaki, Y., Sawano, M., & Kawamura, K. (2014). Low-molecular-weight hydroxyacids in  
629 marine atmospheric aerosol: Evidence of a marine microbial origin. *Biogeosciences*, 11(16),  
630 4407–4414. <https://doi.org/10.5194/BG-11-4407-2014>
- 631 Müller, J.-F., Stavrou, T., Bauwens, M., Compornolle, S., & Peeters, J. (2018). Chemistry  
632 and deposition in the Model of Atmospheric composition at Global and Regional scales using  
633 Inversion Techniques for Trace gas Emissions (MAGRITTE v1.0). Part B. Dry deposition.  
634 <https://doi.org/10.5194/gmd-2018-317>
- 635 Nah, T., Guo, H., Sullivan, A. P., Chen, Y., Tanner, D. J., Nenes, A., Russell, A., Lee Ng, N.,  
636 Gregory Huey, L., & Weber, R. J. (2018). Characterization of aerosol composition, aerosol  
637 acidity, and organic acid partitioning at an agriculturally intensive rural southeastern US site.  
638 *Atmospheric Chemistry and Physics*, 18(15), 11471–11491. [https://doi.org/10.5194/ACP-18-](https://doi.org/10.5194/ACP-18-11471-2018)  
639 11471-2018
- 640 Neeb, P., Sauer, F., Horie, O., & Moortgat, G. K. (1997). Formation of hydroxymethyl  
641 hydroperoxide and formic acid in alkene ozonolysis in the presence of water vapour.  
642 *Atmospheric Environment*, 31(10), 1417–1423. [https://doi.org/10.1016/S1352-](https://doi.org/10.1016/S1352-2310(96)00322-6)  
643 2310(96)00322-6
- 644 Novakov, T., & Penner, J. E. (1993). Large contribution of organic aerosols to cloud-  
645 condensation-nuclei concentrations. *Nature* 1993 365:6449, 365(6449), 823–826.  
646 <https://doi.org/10.1038/365823a0>
- 647 Pan, X., Underwood, J. S., Xing, J.-H., Mang, S. A., & Nizkorodov, S. A. (2009).  
648 Photodegradation of secondary organic aerosol generated from limonene oxidation by ozone  
649 studied with chemical ionization mass spectrometry. *Atmos. Chem. Phys*, 9, 3851–3865.  
650 <https://doi.org/10.5194/acp-9-3851-2009>
- 651 Paulot, F., Crouse, J. D., Kjaergaard, H. G., Kroll, J. H., Seinfeld, J. H., & Wennberg, P. O.  
652 (2009). Isoprene photooxidation: New insights into the production of acids and organic nitrates.  
653 *Atmospheric Chemistry and Physics*, 9(4), 1479–1501. [https://doi.org/10.5194/acp-9-1479-](https://doi.org/10.5194/acp-9-1479-2009)  
654 2009
- 655 Paulot, F., Wunch, D., Crouse, J. D., Toon, G. C., Millet, D. B., Decarlo, P. F., Vigouroux, C.,  
656 Deutscher, N. M., Abad, G. G., Notholt, J., Warneke, T., Hannigan, J. W., Warneke, C., de Gouw,  
657 J. A., Dunlea, E. J., de Mazière, M., Griffith, D. W. T., Bernath, P., Jimenez, J. L., & Wennberg,



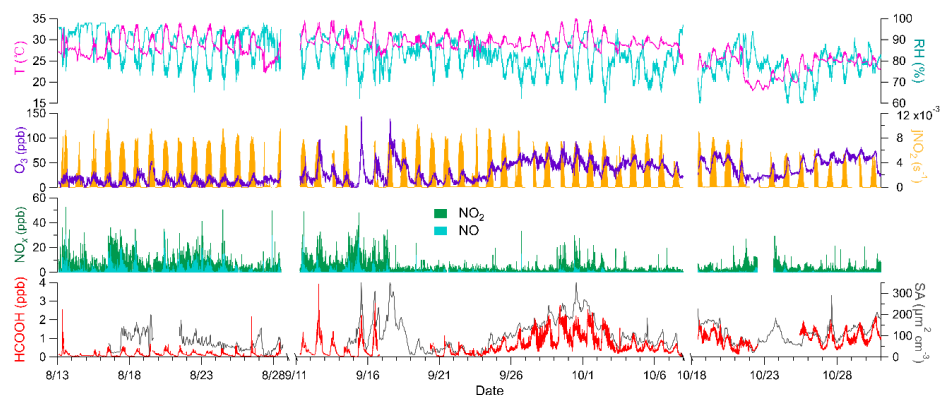
- 658 P. O. (2011). Importance of secondary sources in the atmospheric budgets of formic and acetic  
659 acids. *Atmospheric Chemistry and Physics*, 11(5), 1989–2013. [https://doi.org/10.5194/acp-11-](https://doi.org/10.5194/acp-11-1989-2011)  
660 1989-2011
- 661 Peng, X., Wang, T., Wang, W., Ravishankara, A. R., George, C., Xia, M., Cai, M., Li, Q.,  
662 Salvador, C. M., Lau, C., Lyu, X., Poon, C. N., Mellouki, A., Mu, Y., Hallquist, M., Saiz-Lopez,  
663 A., Guo, H., Herrmann, H., Yu, C., ... Chen, J. (2022). Photodissociation of particulate nitrate  
664 as a source of daytime tropospheric Cl<sub>2</sub>. *Nature Communications*, 13(1).  
665 <https://doi.org/10.1038/s41467-022-28383-9>
- 666 Sanhueza, E., & Andreae, M. O. (1991). Emission of formic and acetic acids from tropical  
667 Savanna soils. *Geophysical Research Letters*, 18(9), 1707–1710.  
668 <https://doi.org/10.1029/91GL01565>
- 669 Saunders, S. M., Jenkin, M. E., Derwent, R. G., & Pilling, M. J. (2003). Protocol for the  
670 development of the Master Chemical Mechanism, MCM v3 (Part A): Tropospheric degradation  
671 of non-aromatic volatile organic compounds. *Atmospheric Chemistry and Physics*, 3(1), 161–  
672 180. <https://doi.org/10.5194/ACP-3-161-2003>
- 673 Shaw, M. F., Sztáray, B., Whalley, L. K., Heard, D. E., Millet, D. B., Jordan, M. J. T., Osborn,  
674 D. L., & Kable, S. H. (2018). Photo-tautomerization of acetaldehyde as a photochemical source  
675 of formic acid in the troposphere. *Nature Communications*, 9(1), 1–7.  
676 <https://doi.org/10.1038/s41467-018-04824-2>
- 677 Franco, B., Blumenstock, T., Cho, C. et al. Ubiquitous atmospheric production of organic acids  
678 mediated by cloud droplets. *Nature* 593, 233–237 (2021). [https://doi.org/10.1038/s41586-021-](https://doi.org/10.1038/s41586-021-03462-x)  
679 03462-x
- 680 Stavrou, T., Müller, J. F., Peeters, J., Razavi, A., Clarisse, L., Clerbaux, C., Coheur, P. F.,  
681 Hurtmans, D., de Mazière, M., Vigouroux, C., Deutscher, N. M., Griffith, D. W. T., Jones, N.,  
682 & Paton-Walsh, C. (2012). Satellite evidence for a large source of formic acid from boreal and  
683 tropical forests. *Nature Geoscience*, 5(1), 26–30. <https://doi.org/10.1038/ngeo1354>
- 684 Su, T., Li, J., Li, C., Xiang, P., Lau, A. K. H., Guo, J., Yang, D., & Miao, Y. (2017). An  
685 intercomparison of long-term planetary boundary layer heights retrieved from CALIPSO,  
686 ground-based lidar, and radiosonde measurements over Hong Kong. *Journal of Geophysical*  
687 *Research: Atmospheres*, 122(7), 3929–3943. <https://doi.org/10.1002/2016JD025937>
- 688 Toda, K., Yunoki, S., Yanaga, A., Takeuchi, M., Ohira, S.-I., & Dasgupta, P. K. (2014).  
689 Formaldehyde Content of Atmospheric Aerosol. <https://doi.org/10.1021/es500590e>
- 690 Vet, R., Artz, R. S., Carou, S., Shaw, M., Ro, C. U., Aas, W., Baker, A., Bowersox, V. C.,  
691 Dentener, F., Galy-Lacaux, C., Hou, A., Pienaar, J. J., Gillett, R., Forti, M. C., Gromov, S.,  
692 Hara, H., Khodzher, T., Mahowald, N. M., Nickovic, S., ... Reid, N. W. (2014). A global  
693 assessment of precipitation chemistry and deposition of sulfur, nitrogen, sea salt, base cations,  
694 organic acids, acidity and pH, and phosphorus. *Atmospheric Environment*, 93, 3–100.  
695 <https://doi.org/10.1016/J.ATMOENV.2013.10.060>



- 696 Walser, M. L., Park, J., Gomez, A. L., Russell, A. R., & Nizkorodov, S. A. (2007).  
697 Photochemical Aging of Secondary Organic Aerosol Particles Generated from the Oxidation  
698 of d-Limonene. <https://doi.org/10.1021/jp0662931>
- 699 Wolfe, G. M., Marvin, M. R., Roberts, S. J., Travis, K. R., & Liao, J. (2016). The framework  
700 for 0-D atmospheric modeling (F0AM) v3.1. *Geoscientific Model Development*, 9(9), 3309–  
701 3319. <https://doi.org/10.5194/GMD-9-3309-2016>
- 702 Xia, K., Tong, S., Zhang, Y., Tan, F., Chen, Y., Zhang, W., Guo, Y., Jing, B., Ge, M., Zhao, Y.,  
703 Alamry, K. A., Marwani, H. M., & Wang, S. (2018). Heterogeneous Reaction of HCOOH on  
704 NaCl Particles at Different Relative Humidities. *Journal of Physical Chemistry A*, 122(36),  
705 7218–7226. <https://doi.org/10.1021/ACS.JPCA.8B02790>
- 706 Xia, M., Wang, T., Wang, Z., Chen, Y., Peng, X., Huo, Y., Wang, W., Yuan, Q., Jiang, Y., Guo,  
707 H., Lau, C., Leung, K., Yu, A., & Lee, S. (2022). Pollution-Derived Br<sub>2</sub> Boosts Oxidation  
708 Power of the Coastal Atmosphere. <https://doi.org/10.1021/acs.est.2c02434>
- 709 Xu, J., Chen, J., Shi, Y., Zhao, N., Qin, X., Yu, G., Liu, J., Lin, Y., Fu, Q., Weber, R. J., Lee, S.  
710 H., Deng, C., & Huang, K. (2020). First Continuous Measurement of Gaseous and Particulate  
711 Formic Acid in a Suburban Area of East China: Seasonality and Gas-Particle Partitioning. *ACS*  
712 *Earth and Space Chemistry*, 4(2), 157–167.  
713 <https://doi.org/10.1021/acsearthspacechem.9b00210>
- 714 Ye, C., Zhang, N., Gao, H., & Zhou, X. (2017). Photolysis of Particulate Nitrate as a Source of  
715 HONO and NO<sub>x</sub>. *Environmental Science and Technology*, 51(12), 6849–6856.  
716 <https://doi.org/10.1021/acs.est.7b00387>
- 717 Yokelson, R. J., Crouse, J. D., DeCarlo, P. F., Karl, T., Urbanski, S., Atlas, E., Campos, T.,  
718 Shinozuka, Y., Kapustin, V., Clarke, A. D., Weinheimer, A., Knapp, D. J., Montzka, D. D.,  
719 Holloway, J., Weibring, P., Flocke, F., Zheng, W., Toohey, D., Wennberg, P. O., ... Shetter, R.  
720 (2009). Emissions from biomass burning in the Yucatan. *Atmospheric Chemistry and Physics*,  
721 9(15), 5785–5812. <https://doi.org/10.5194/ACP-9-5785-2009>
- 722 Yu, S. (2000). Role of organic acids (formic, acetic, pyruvic and oxalic) in the formation of  
723 cloud condensation nuclei (CCN): a review. *Atmospheric Research*, 53(4), 185–217.  
724 [https://doi.org/10.1016/S0169-8095\(00\)00037-5](https://doi.org/10.1016/S0169-8095(00)00037-5)
- 725 Yuan, B., Veres, P. R., Warneke, C., Roberts, J. M., Gilman, J. B., Koss, A., Edwards, P. M.,  
726 Graus, M., Kuster, W. C., Li, S. M., Wild, R. J., Brown, S. S., Dubé, W. P., Lerner, B. M.,  
727 Williams, E. J., Johnson, J. E., Quinn, P. K., Bates, T. S., Lefter, B., ... de Gouw, J. A. (2015).  
728 Investigation of secondary formation of formic acid: Urban environment vs. oil and gas  
729 producing region. *Atmospheric Chemistry and Physics*, 15(4), 1975–1993.  
730 <https://doi.org/10.5194/acp-15-1975-2015>
- 731 Zellner, R., Exner, M., & Herrmann, H. (1990). Absolute OH quantum yields in the laser  
732 photolysis of nitrate, nitrite and dissolved H<sub>2</sub>O<sub>2</sub> at 308 and 351 nm in the temperature range  
733 278–353 K. *Journal of Atmospheric Chemistry*, 10(4), 411–425.



- 734 <https://doi.org/10.1007/BF00115783>
- 735 Zervas, E., Montagne, X., & Lahaye, J. (2001a). C1–C5 Organic Acid Emissions from an SI  
736 Engine: Influence of Fuel and Air/Fuel Equivalence Ratio. *Environmental Science and*  
737 *Technology*, 35(13), 2746–2751. <https://doi.org/10.1021/ES000237V>
- 738 Zervas, E., Montagne, X., & Lahaye, J. (2001b). Emission of specific pollutants from a  
739 compression ignition engine. Influence of fuel hydrotreatment and fuel/air equivalence ratio.  
740 *Atmospheric Environment*, 35(7), 1301–1306. [https://doi.org/10.1016/S1352-2310\(00\)00390-](https://doi.org/10.1016/S1352-2310(00)00390-3)  
741 3
- 742 Zhang, R., Gen, M., Fu, T. M., & Chan, C. K. (2021). Production of Formate via Oxidation of  
743 Glyoxal Promoted by Particulate Nitrate Photolysis. *Environmental Science and Technology*,  
744 55(9), 5711–5720. <https://doi.org/10.1021/acs.est.0c08199>
- 745 Zhang, R., Suh, I., Zhao, J., Zhang, D., Fortner, E. C., Tie, X., Molina, L. T., & Molina, M. J.  
746 (2004). Atmospheric New Particle Formation Enhanced by Organic Acids. *New Series*,  
747 304(5676), 1487–1490. <https://doi.org/10.1126/science.1095139>
- 748 Zhu, C., Xiang, B., Zhu, L., & Cole, R. (2008). Determination of absorption cross sections of  
749 surface-adsorbed HNO<sub>3</sub> in the 290–330 nm region by Brewster angle cavity ring-down  
750 spectroscopy. *Chemical Physics Letters*, 458(4–6), 373–377.  
751 <https://doi.org/10.1016/j.cplett.2008.04.125>
- 752



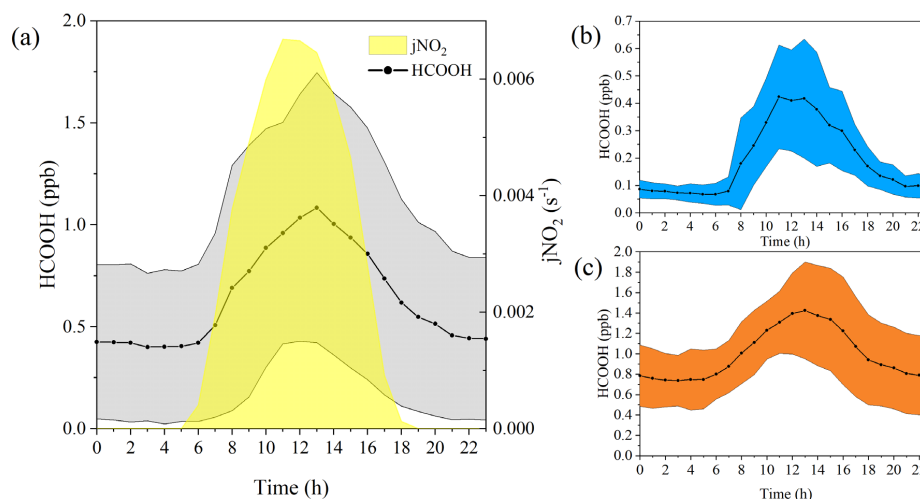
753

754 **Fig. 1** Times series of temperature (T); relative humidity (RH); nitrogen dioxide photolysis  
 755 frequency ( $j\text{NO}_2$ ); concentrations of ozone ( $\text{O}_3$ ), nitrogen oxides ( $\text{NO}_x$ ), and formic acid  
 756 ( $\text{HCOOH}$ ); and surface area density (SA) during the field campaign. Data were not collected  
 757 from August 29 to September 10 due to the persistently clean weather conditions, similar to  
 758 those during the initial stage of the campaign. The gap in data collection from October 8 to  
 759 October 17 was due to a rainstorm. Any other short gaps were caused by instrument  
 760 maintenance.

761 **Table 1.** Summary of worldwide field-observed formic acid ( $\text{HCOOH}$ ) concentrations

Location	Type	Time	$\text{HCOOH}$ (ppb)	Reference
Pasadena, USA	urban	2010.06-07	$2.0 \pm 1.0$	(Yuan et al., 2015)
Kensington,	urban	2012.01-02	0.63 (winter)	(Bannan et al., 2017)
London	background	2012.07-08	1.33 (summer)	
Shanghai, China	suburban	2017.06.18-12.23	$2.08 \pm 1.89$	(Xu et al., 2020)
Yorkville, USA	rural	2016.08.15-10.13	$1.17 \pm 0.85$	(Nah et al., 2018)
North Pacific	marine	2008.07.29-08.19	$30 \pm 39.8$ ppt	(Miyazaki et al., 2014)
Pacific and Atlantic	marine	2017.09-10	< 0.1	(Chen et al., 2021)
Colorado, USA	forest	2016.02.01-03.01	$55 \pm 57$ ppt (winter)	(Fulgham et al., 2019)
		2016.04.15-05.15	$30 \pm 24$ ppt (spring)	
		2016.07.15-08.15	$1.2 \pm 0.91$ (summer)	
		2016.10.01-11.01	$0.81 \pm 0.48$ (autumn)	
Alabama, USA	deciduous forest	2013.06-07	2.5 (peak average daytime)	(Millet et al., 2015)
Hong Kong, China	coastal	2021.08.13-10.31	$0.58 \pm 0.53$	This study

762



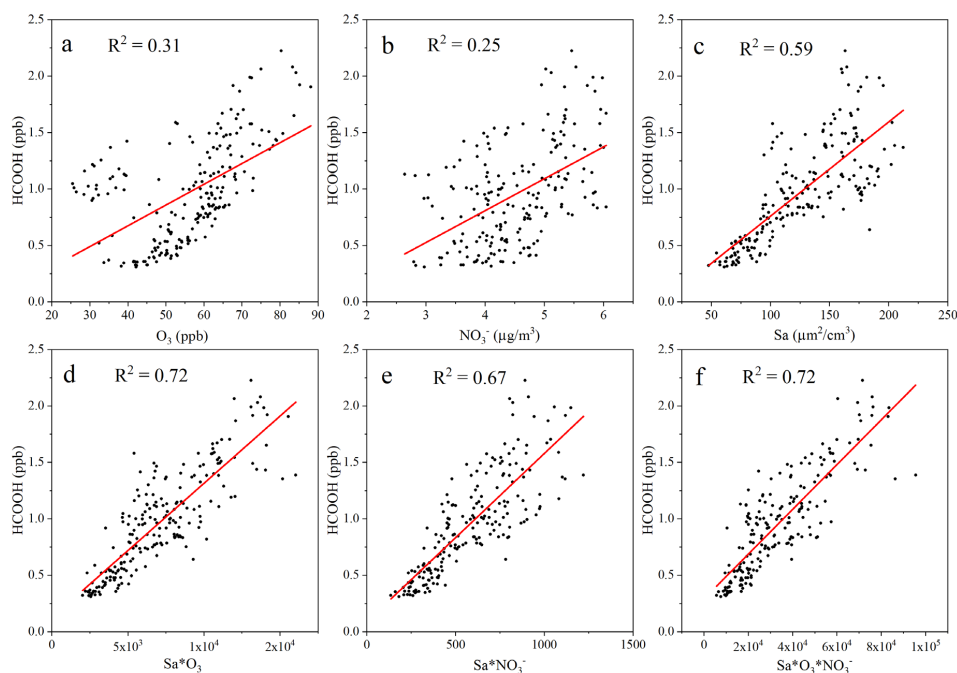
763

764 **Fig. 2** Diurnal variation in the concentrations of formic acid (HCOOH) in different periods. (a)  
 765 Diurnal cycle of HCOOH concentrations and frequency of nitrogen dioxide photolysis ( $j\text{NO}_2$ )  
 766 for the whole campaign; (b) and (c) diurnal cycle of HCOOH concentrations in marine and  
 767 coastal air masses, respectively. The shading represents the standard deviations of the  
 768 measurements.

769 **Table 2.** Pearson correlation coefficient  $\rho$  matrix between the concentration of formic acid and  
 770 other air pollutants, and related meteorological parameters, during three distinct periods.

Parameter	Coastal	Haze	Marine	Parameter	Coastal	Haze	Marine
$j\text{NO}_2$	0.41	0.58	0.65	Sa	0.73	0.68	-0.03
T	-0.27	0.70	0.72	$\text{Sa} \times \text{NO}_3^-$	0.85	0.56	0.15
RH	-0.56	-0.51	-0.65	$\text{Sa} \times \text{O}_3$	0.83	0.74	0.31
$\text{PM}_{10}$	0.79	0.66	0.05	$\text{HNO}_3$	0.75	0.59	0.69
$\text{PM}_{2.5}$	0.69	0.63	0.19	$\text{Cl}^-$	-0.41	-0.44	0.09
$\text{PM}_{10}$	0.68	0.55	0.26	$\text{NO}_3^-$	0.67	-0.10	0.57
HONO	-0.03	0.26	-0.34	$\text{SO}_4^{2-}$	0.66	0.65	0.10
$\text{CH}_3\text{COOH}$	0.89	0.88	-0.27	$\text{Na}^+$	-0.28	-0.50	0.37
NO	-0.12	0.44	0.13	$\text{NH}_4^+$	0.72	0.64	0.24
$\text{NO}_2$	-0.24	0.36	-0.39	$\text{K}^+$	0.53	0.32	0.15
$\text{NO}_x$	-0.22	0.40	-0.27	$\text{Mg}^{2+}$	-0.30	-0.38	0.47
$\text{O}_3$	0.69	0.65	0.68	$\text{Ca}^{2+}$	-0.11	0.09	0.04
$\text{SO}_2$	0.64	0.66	0.41	HCl	0.18	0.51	0.55
CO	0.63	0.51	0.13	isoprene	0.03	0.61	0.63
$\text{NH}_3$	0.37	0.46	0.16	benzene	0.63	0.55	0.05

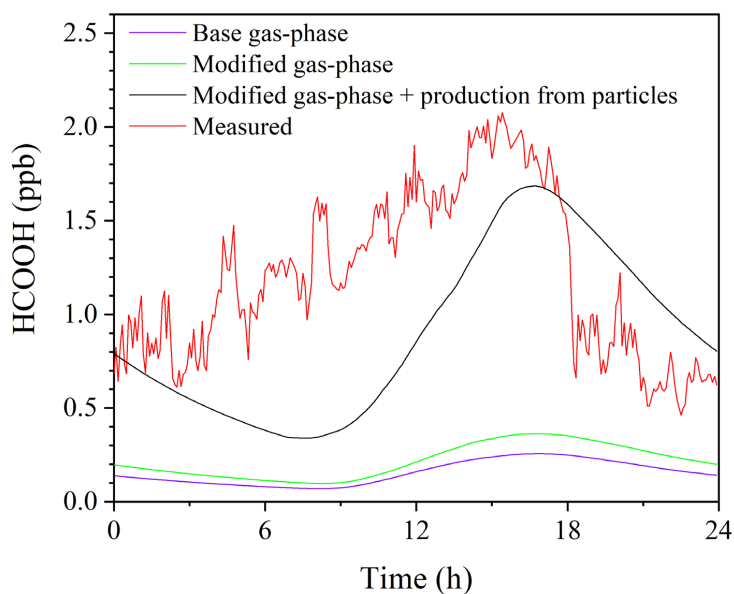
771



772

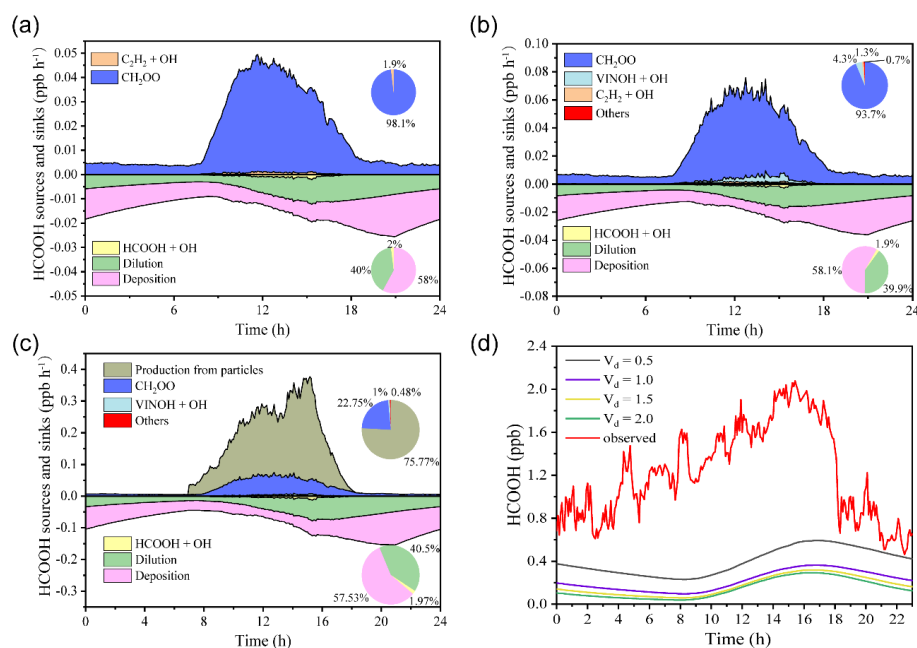
773 **Fig. 3** Scatter plot of the concentration of formic acid (HCOOH) and (a) the concentration of  
 774 ozone (O<sub>3</sub>); (b) the mass concentration of nitrate ions (NO<sub>3</sub><sup>-</sup>) in PM<sub>2.5</sub>; (c) the surface  
 775 area density (Sa) of PM<sub>1</sub> (µm<sup>2</sup> cm<sup>-3</sup>); (d) the product of Sa and the concentration of O<sub>3</sub>; (e) the  
 776 product of Sa and the concentration of NO<sub>3</sub><sup>-</sup>; and (f) the product of Sa, the concentration of O<sub>3</sub>,  
 777 and the concentration of NO<sub>3</sub><sup>-</sup> in coastal air masses.





778

779 **Fig. 4** Variations in the concentrations of formic acid (HCOOH) on 28 September 2021.

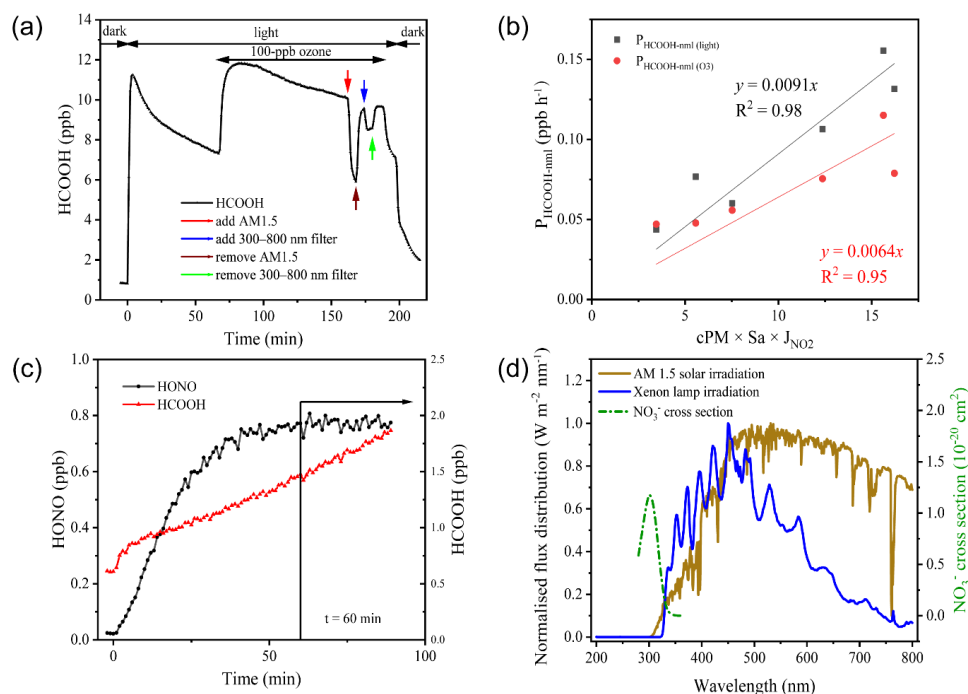


780

781 **Fig. 5** Model-calculated profiles of sources and sinks of formic acid (HCOOH) on 28  
 782 September 2021 for (a) the base case; (b) the modified case; and (c) the case including the  
 783 production from particles. Upper right inset: the contribution from various sources to HCOOH  
 784 concentrations. Bottom right inset: the contribution from different sinks to HCOOH



785 concentrations.  $\text{CH}_2\text{OO}$  = formaldehyde oxide, a Criegee intermediate (biradical);  $\text{VINOH}$  =  
 786 vinyl alcohol. d) Model-predicted concentrations of  $\text{HCOOH}$  based on various deposition  
 787 velocities ( $V_d$ ).



788  
 789 **Fig. 6** Results of the irradiation experiments. (a) Typical variation in formic acid ( $\text{HCOOH}$ )  
 790 concentrations during irradiation (in aerosols collected on 2 November 2020). AM 1.5 and  
 791 300–800 nm filters were added after the addition of 100-ppb ozone. (b) The correlation between  
 792  $P_{\text{HCOOH-nmi}}$  and 2.5- $\mu\text{m}$  particulate matter ( $\text{PM}_{2.5}$ ) concentration ( $\text{cPM}$ )  $\times$  surface area ( $\text{Sa}$ )  $\times$   
 793 nitrogen dioxide photolytic frequency ( $J_{\text{NO}_2}$ ). (c) Variations in the concentrations of  $\text{HCOOH}$   
 794 and nitrous acid ( $\text{HONO}$ ) as a function of time after illumination of an aqueous solution of  
 795 formaldehyde and sodium nitrite at  $\text{pH} = 2.7$ . The vertical black line indicates the time at which  
 796  $\text{HONO}$  stabilised. (d) Comparison of the irradiation spectrum of the xenon lamp used in this  
 797 study and standard air mass 1.5 solar irradiation (AM 1.5).

798



799 **Table 3** Summary of formic acid (HCOOH) concentrations and production rates observed in  
800 chamber experiments and normalised HCOOH production rates in ambient air under light and  
801 light + ozone (O<sub>3</sub>) conditions, respectively. HCOOH<sub>(O<sub>3</sub>)</sub> denotes the increased concentration of  
802 HCOOH after the addition of 100 ppb O<sub>3</sub>.

Date	HCOOH <sub>(light)</sub> (ppt)	HCOOH <sub>(O<sub>3</sub>)</sub> (ppt)	P <sub>HCOOH(light)</sub> (ppt s <sup>-1</sup> )	P <sub>HCOOH(O<sub>3</sub>)</sub> (ppt s <sup>-1</sup> )	P <sub>HCOOH-nml (light)</sub> (ppb h <sup>-1</sup> )	P <sub>HCOOH-nml (O<sub>3</sub>)</sub> (ppb h <sup>-1</sup> )
2020.10.07	8420.2	4670.0	299.4	166.0	1.70E-01	1.33E-01
2020.10.08	6787.7	2899.0	241.3	103.1	1.31E-01	7.89E-02
2020.10.26	4660.9	3077.5	165.7	109.4	6.01E-02	5.57E-02
2020.11.02	6656.3	3507.6	236.7	124.7	1.55E-01	1.15E-01
2020.11.03	4490.8	2266.7	159.7	80.6	1.06E-01	7.55E-02
2020.11.04	4943.1	2191.5	175.8	77.9	7.67E-02	4.77E-02
2020.11.05	3088.0	2368.6	109.8	84.2	4.37E-02	4.71E-02
Average	5578.1	2997.3	198.3	106.6	1.06E-01	7.89E-02

803